

CrossMark
click for updates

Cite this: DOI: 10.1039/c6ta04503k

Low-temperature plasma-enhanced atomic layer deposition of tin oxide electron selective layers for highly efficient planar perovskite solar cells†

Changlei Wang,^{‡,ab} Dewei Zhao,^{‡,*a} Corey R. Grice,^a Weiqiang Liao,^a Yue Yu,^a Alexander Cimaroli,^a Niraj Shrestha,^a Paul J. Roland,^a Jing Chen,^c Zhenhua Yu,^b Pei Liu,^b Nian Cheng,^b Randy J. Ellingson,^a Xingzhong Zhao^{*b} and Yanfa Yan^{*a}

Recent progress has shown that low-temperature processed tin oxide (SnO₂) is an excellent electron selective layer (ESL) material for fabricating highly efficient organic–inorganic metal-halide perovskite solar cells with a planar cell structure. Low-temperature processing and a planar cell structure are desirable characteristics for large-scale device manufacturing due to their associated low costs and processing simplicity. Here, we report that plasma-enhanced atomic layer deposition (PEALD) is able to lower the deposition temperature of SnO₂ ESLs to below 100 °C and still achieve high device performance. With C₆₀-self-assembled monolayer passivation, our PEALD SnO₂ ESLs deposited at ~100 °C led to average power conversion efficiencies higher than 18% (maximum of 19.03%) and 15% (maximum of 16.80%) under reverse voltage scan for solar cells fabricated on glass and flexible polymer substrates, respectively. Our results thus demonstrate the potential of the low-temperature PEALD process of SnO₂ ESLs for large-scale manufacturing of efficient perovskite solar cells.

Received 31st May 2016

Accepted 9th July 2016

DOI: 10.1039/c6ta04503k

www.rsc.org/MaterialsA

Introduction

Organic–inorganic lead halide perovskite solar cells (PVSCs) have attracted much attention in the past few years since their power conversion efficiency (PCE) has increased from 3.8% (ref. 1) to over 22%.^{2–4} Such a rapid improvement of efficiency is ascribed to the superior photovoltaic properties of these halide perovskite materials such as high optical absorption coefficients with a broad absorption range,⁵ weak exciton binding energy,⁶ long carrier lifetime and charge diffusion length,⁷ and benign defect properties,^{8–13} as well as ease of fabrication.^{2,14–21} Additionally, since lead halide perovskites exhibit excellent electron and hole transport properties,²² efficient PVSCs can be fabricated by simply sandwiching a perovskite absorber between an electron selective layer (ESL) and a hole selective layer (HSL).^{23,24} The record efficiency PVSCs are realized using mesoporous TiO₂ ESLs,^{2,3} which require sintering at

temperatures above 450 °C.²⁵ For large-scale roll-to-roll manufacturing, a simple planar cell structure and low-temperature processing are highly preferred. Other transition metal oxides such as ZnO (ref. 26 and 27) and SnO₂ (ref. 28–31) have also been explored as potential ESL materials for PVSCs. Both compact ZnO and SnO₂ thin films can be deposited by low-temperature processes. The electron mobilities of ZnO (ref. 32) and SnO₂ (ref. 33) were reported to be much higher than that of TiO₂. Planar PVSCs using ZnO, Zn₂SnO₄, and SnO₂ ESLs have achieved high PCEs.^{26,29,31,34,35} It is worth mentioning that lead halide perovskites deposited on ZnO ESLs are thermally unstable,³⁶ suffering from fast decomposition to PbI₂ when annealed up to 80 °C.³⁷ Moreover, low-temperature processed SnO₂ ESLs have shown some advantages over compact TiO₂ ESLs including better cell stability,³⁸ higher optical transparency,³³ and barrier-free energetic configuration.^{30,38} Furthermore, if a SnO₂ layer is grown on the top of thin-film solar cells, it can improve the stability of the cells against moisture.³⁹

Low-temperature SnO₂ ESLs have been deposited by various methods including spin-coating,^{28,31,33,34} dual-fuel combustion,²⁹ and thermal ozone atomic-layer deposition (ALD),³⁸ among which ALD is expected to produce the most compact thin films at the lowest deposition temperature.⁴⁰ SnO₂ ESLs grown by ozone ALD at a temperature close to 120 °C have produced PVSCs with PCEs of over 18%, indicating that ALD is a promising method for obtaining effective ESLs.³⁸ However, further reduction in the deposition temperature while

^aDepartment of Physics and Astronomy, Wright Center for Photovoltaics Innovation and Commercialization, The University of Toledo, Toledo, OH 43606, USA. E-mail: dewei_zhao@hotmail.com; Yanfa.Yan@utoledo.edu

^bKey Laboratory of Artificial Micro/Nano Structures of Ministry of Education, School of Physics and Technology, Wuhan University, Wuhan 430072, China. E-mail: xzzhao@whu.edu.cn

^cSchool of Electronic Science and Engineering, Southeast University, Nanjing 210096, China

† Electronic supplementary information (ESI) available. See DOI: 10.1039/c6ta04503k

‡ These authors contributed equally to this work.

maintaining high-efficiency device performance could be even more beneficial for large-scale PVSC fabrication, especially for flexible PVSCs.^{35,41–43} In a thermal ALD process, the reaction of the metal precursor relies on the deposition temperature. Compared with thermal ALD, plasma-enhanced ALD (PEALD) has demonstrated the ability to deposit films with equivalent material properties at lower substrate temperatures due to the higher reactivity enhanced by the plasma species.^{44,45} Therefore, PEALD is a method of choice for further lowering the processing temperature of SnO₂ ESLs.

In this work, we demonstrate that the deposition temperature of SnO₂ ESLs that results in the best device performance can be reduced to ~100 °C using PEALD. After passivating the surface of SnO₂ ESLs with a C₆₀-self-assembled monolayer (C₆₀-SAM),^{29,46,47} PVSCs fabricated on glass and flexible substrates have achieved average power conversion efficiencies (PCEs) higher than 18% (maximum of 19.03%) and 15% (maximum of 16.80%), respectively. It is worth noting that even the SnO₂ ESLs deposited by PEALD at 70 °C are able to generate PVSCs with average PCEs over 17%. Therefore, our results demonstrate the potential of PEALD for synthesizing high-quality SnO₂ ESLs at very low temperature to fabricate highly efficient perovskite solar cells.

Experimental

Plasma-enhanced ALD SnO₂ deposition

FTO glass with a sheet resistance of 15 Ω □⁻¹ was cleaned with a chemical detergent, facilitated by ultrasonication, with water, acetone and iso-propanol successively prior to PEALD of SnO₂. An ITO/PET (45 Ω □⁻¹) substrate was cleaned by the same procedure. Tetrakis(dimethylamino)-tin(IV) (99%, TDMA-Sn, Strem Chemicals Inc.) was used as the Sn precursor and pure O₂ (ultra-high pure, Airgas) was used as the oxidizer. Ar (ultra-high pure, Airgas) was used as the carrier gas with a flow rate of 15 sccm. PEALD SnO₂ was deposited at 100 °C with an Ensure Scientific Group AutoALD-PE V2.0 equipped with a plasma generator. The TDMA-Sn precursor was held at 75 °C. The resulting deposition rate is about 1.7 Å per cycle as determined by spectroscopic ellipsometry.

Perovskite precursor preparation

A 45% by weight precursor solution was prepared with lead iodide (PbI₂, Alfa Aesar, 99.9985%) and methylammonium iodide (MAI) (molar ratio = 1 : 1) in *N,N*-dimethylformamide (DMF) and dimethyl sulfoxide (DMSO) (volume ratio = 9 : 1). A small amount of lead thiocyanate (Pb(SCN)₂, Sigma-Aldrich, 99.5%) was added into the precursor solution as an additive.^{48,49} It has been shown that the Pb(SCN)₂ additive can enlarge the grain size of the resulting perovskite thin films and subsequently improve the cell performance. The solution was stirred for 12 hours on a 60 °C hot plate before deposition.

Solar cell fabrication

The C₆₀-SAM was purchased and used without further purification. The C₆₀-SAM at a concentration of 4 mg mL⁻¹ was

dissolved in chlorobenzene (Sigma-Aldrich, 99.8%) under vigorous stirring overnight. The C₆₀-SAM was then deposited onto the SnO₂ ESL by a spin coating method as previously reported.²⁹ The perovskite precursor solution was spin-coated on the C₆₀-SAM/SnO₂ ESLs first at 500 rpm for 3 s and then at 4000 rpm for 60 s using an anti-solvent technique.^{48,50} Diethyl ether, as the anti-solvent agent, was then drop-cast on the substrate. After spin coating, the perovskite film was annealed at 65 °C for 2 minutes and then at 100 °C for 5 minutes. All of these processes were carried out in a N₂ filled glove box. Spiro-OMeTAD (Shenzhen Feiming Science and Technology Co., Ltd., 99.0%) was used as the HSL and deposited on the perovskite film at 2000 rpm for 60 seconds. The Spiro-OMeTAD solution was prepared by dissolving 72.3 mg Spiro-OMeTAD in 1 mL chlorobenzene with 28 μL 4-*tert*-butylpyridine (TBP) (Sigma-Aldrich, 96%) and 18 μL Li-bis(trifluoromethanesulfonyl)imide (Li-TFSI) (Sigma-Aldrich, 99.95%) (520 mg mL⁻¹ in acetonitrile). A layer of 80 nm gold (Au) was then deposited on the top of Spiro-OMeTAD using thermal evaporation. The working area of the devices was 0.08 cm² as defined by a shadow mask during the Au evaporation.

Perovskite device characterization

Current density–voltage (*J*–*V*) curves were obtained under standard AM 1.5 G illumination using a solar simulator (PV Measurements, Inc) equipped with a 450 W xenon lamp with an output intensity of 100 mW cm⁻² calibrated with a reference Si cell at the measurement location. The light intensity was later adjusted between 0.5 and 100 mW cm⁻² using neutral density filters. EQE measurements were carried out with an EQE system (PV Measurements, Inc) using 100 Hz chopped monochromatic light ranging from 300 nm to 900 nm under otherwise near-dark test conditions. Transmission spectra and ultraviolet-visible absorbance spectra were measured with an ultraviolet-visible spectrophotometer (CARY5000, Varian, Australia). Impedance spectra were recorded on an electrochemical workstation (Votlab PGZ-301) at 0 mV bias in the dark. The plane view and cross sectional structures of the substrates and PVSCs were characterized with a field emission SEM instrument (Hitachi S-4800). The crystallinity and the crystal structure of the perovskite layer were analyzed with an Ultima III X-ray diffractometer using a Ni-filtered Cu K α X-ray source (Rigaku Corp.). The film thickness was analyzed *via* spectroscopic ellipsometry using a single rotating compensator multichannel ellipsometer (Model M2000FI, J. A. Woollam Co., Inc.). AFM was carried out with a Nanoscope V atomic force microscope operating in the tapping-mode (Veeco Metrology Group). The sheet resistance was measured using a four-point probe method resistivity test system (PRO4-440N, Lucas labs).

Steady-state and time resolved photoluminescence measurements

PL and TRPL measurements were performed at room temperature in ambient air. The samples were excited through the glass side (*i.e.* ESL side). For steady-state PL, a 532 nm cw laser (intensity = 11 mW cm⁻², beam diameter \approx 140 μm) was used

as a source of excitation. The PL signal was detected with a Symphony-II CCD (from Horiba) detector after a 300 g mm⁻¹ grating monochromator (integration time = 0.5 s). Time resolved photoluminescence measurements were performed using a time correlated single photon counting module (Becker & Hickel Simple Tau SPCM 130-E/M module). A 532 nm pulsed laser (0.2 mW cm⁻², beam diameter ≈ 100 μm) was used as a source of excitation. The photoluminescence signal was dispersed with a Horiba IHR 320 monochromator (grating 900 g mm⁻¹, 850 nm blaze, and detected with a hybrid APD/PMT module (Hamamatsu R10467U-50)). TRPL measurements were performed (integration time = 1200 s) at a 1 MHz repetition rate. TCSPC decay curves obtained in the TRPL measurements were fit to two-exponential decay by iterative re-convolution with the measured system response function (W). The mean photogenerated carrier life time is calculated by the weighted average as follows:

$$y(t) = (W \times f)(t)$$

$$f(t) = A_1 \times e^{-\frac{t}{\tau_1}} + A_2 \times e^{-\frac{t}{\tau_2}}$$

$$\text{Mean life time} = \langle \tau \rangle = \frac{A_1 \tau_1^2 + A_2 \tau_2^2}{A_1 \tau_1 + A_2 \tau_2}$$

Results and discussion

Since an ESL layer plays dual roles, *i.e.*, transferring electrons and blocking holes, a pinhole-free and compact film morphology is highly desirable for suppressing the charge recombination at the interfaces.^{51,52} Fig. 1 shows a top-view scanning electron microscopy (SEM) image of PEALD SnO₂ deposited at 100 °C with 130 reaction cycles on a fluorine-doped SnO₂ (FTO) coated glass substrate. The top-view SEM images of bare FTO and FTO coated with PEALD SnO₂ with various reaction cycles are shown in Fig. S1.† The SEM images show that PEALD SnO₂ films are uniformly coated on the surface of FTO.

We used spectroscopic ellipsometry to determine the actual thickness of PEALD deposited SnO₂ ESLs with various reaction

cycles. The thickness–reaction cycle relationship is plotted in Fig. S2.† The thickness increases linearly with the number of reaction cycles. The film thickness for the 130 reaction cycle sample at a deposition temperature of 100 °C is about 15 nm. The PEALD SnO₂ ESLs were also found to exhibit excellent optical properties. As shown in Fig. 1(b), the PEALD SnO₂ ESLs demonstrate antireflection properties, *i.e.*, enhanced transparency across most of the visible spectrum range after PEALD deposition of SnO₂ ESLs compared to the bare FTO substrate. The increased transparency is beneficial for light harvesting by the perovskite layer. This improvement in transparency is consistent with that observed by using SnO₂ ESLs deposited by low-temperature solution processes.³³ PEALD SnO₂ ESLs deposited at temperatures ranging from 50 to 200 °C and reaction cycles ranging from 40 to 190 showed a compact surface morphology and optical transparency, which are suitable properties and necessary requirements for efficient ESLs.

We systematically examined the relationship of the PEALD deposition temperature and the number of reaction cycles with PVSC performance. We used a regular device structure of glass/FTO/PEALD-SnO₂/C₆₀-SAM/perovskite/HSL/Au. The HSL is lithium doped 2,2',7,7'-tetrakis(*N,N'*-di-*p*-methoxyphenylamine)-9,9'-spirobifluorene (Spiro-OMeTAD). As reported in the literature, applying a very thin fullerene layer, such as C₆₀,^{51,52} phenyl-C₆₁-butyric acid methyl ester (PCBM),⁴⁸ and C₆₀-SAMs,^{29,47} can passivate the surfaces of metal oxides and effectively promote charge transfer at the metal oxide ESL/perovskite interfaces. Therefore, we applied a thin C₆₀-SAM interlayer *via* spin-coating for all our PEALD SnO₂ ESLs (Fig. S3†). As seen in Fig. S4,† applying the thin C₆₀-SAM interlayer improves the open-circuit voltage (V_{OC}), short-circuit current density (J_{SC}) and fill factor (FF) and therefore the over-all performance. Meanwhile, the current density–voltage (J – V) hysteresis is reduced with the use of the C₆₀-SAM, which results in improved agreement between the forward and reverse scan values of V_{OC} , J_{SC} , FF and PCE as shown in Fig. S4.† The CH₃NH₃PbI₃ (MAPbI₃) perovskite absorber layers were deposited as described above.^{48,50} The MAPbI₃ perovskite layers deposited on C₆₀-SAM/SnO₂/FTO substrates exhibited high crystallinity and a smooth surface morphology (Fig. S5 and S6†). In Fig. S6(b),† the SEM image displays some relatively brighter particles located at the grain boundaries between the larger MAPbI₃ crystals, which can be ascribed to excessive PbI₂ as we previously reported.⁴⁸ The XRD pattern also confirmed the presence of excess PbI₂ (Fig. S6(a)†).

For better insight into the function of the C₆₀-SAM, steady-state photoluminescence (PL) quenching and time-resolved photoluminescence (TRPL) measurements were performed to evaluate the charge carrier extraction properties.^{3,30} Fig. 2(a) shows that the perovskite film deposited on C₆₀-SAM/SnO₂/FTO has greater PL quenching as compared to the SnO₂/FTO counterpart. Moreover, Fig. 2(b) shows the TRPL of the perovskite films on SnO₂/FTO with and without the C₆₀-SAM. The perovskite film on C₆₀-SAM/SnO₂/FTO shows a faster PL decay than that on SnO₂/FTO. The photogenerated charge carrier lifetimes are estimated to be 22 ns and 57 ns, respectively. This shows that electron extraction can be enhanced by modifying

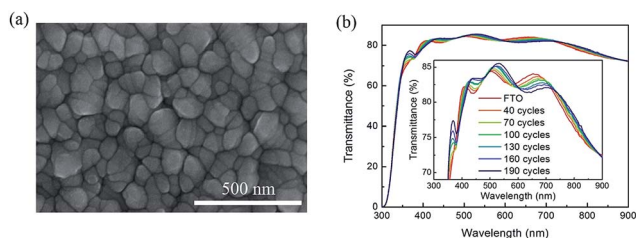


Fig. 1 (a) SEM image of PEALD SnO₂ deposited at 100 °C on a FTO substrate. (b) Transmittance spectra of PEALD SnO₂ films deposited at 100 °C with various reaction cycles on an FTO substrate. The inset in (b) shows an enlarged view of the transmittance spectra in the visible range.

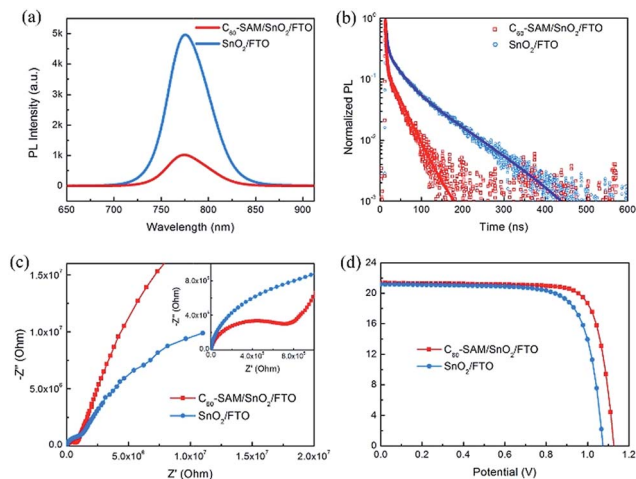


Fig. 2 (a) Steady-state photoluminescence spectra and (b) photoluminescence decay of perovskite films on C_{60} -SAM/ SnO_2 /FTO and SnO_2 /FTO substrates. (c) Impedance spectra and (d) J - V curves of PVSCs based on C_{60} -SAM/ SnO_2 /FTO and SnO_2 /FTO substrates.

perovskite/ SnO_2 contact with the C_{60} -SAM. Impedance spectroscopy (IS) was used to investigate interface charge transport and recombination in our PVSCs.^{20,21,33} Fig. 2(c) shows the Nyquist plots of PVSCs employing C_{60} -SAM/ SnO_2 /FTO and SnO_2 /FTO as ESLs. The semicircle in the low frequency range can be attributed to the recombination resistance (R_{rec}) at the interface of the perovskite and ESL. It is obvious that the R_{rec} is significantly decreased after C_{60} -SAM passivation, indicating reduced recombination. Furthermore, the semicircle in the high frequency range can be attributed to the transfer resistance (R_{tr}) at the perovskite/ESL interface. A lower R_{tr} was obtained in the presence of the C_{60} -SAM, manifesting faster charge transfer at the optimized perovskite/ESL interface and favorable transport of photogenerated generated electrons. The larger R_{rec} and lower R_{tr} should lead to a higher V_{OC} and FF, which is consistent with our J - V results in Fig. 2(d). The V_{OC} , J_{SC} , FF and PCE of PVSCs based on C_{60} -SAM/ SnO_2 /FTO are 1.126 V, 21.35 $mA\ cm^{-2}$, 79.10% and 19.02%, while those of PVSCs based on SnO_2 /FTO are 1.074 V 21.17 $mA\ cm^{-2}$, 75.48% and 17.16%, respectively. The higher V_{OC} and FF are ascribed to efficient electron extraction and hole blocking of the C_{60} -SAM.

We first explored the performance dependence on reaction cycles of 40, 70, 100, 130, 160, and 190; all with the deposition temperature at 100 °C. Their corresponding thicknesses can be found in Fig. S2.† The J - V curves of some representative PVSCs using PEALD SnO_2 ESLs with various reaction cycles, measured under both reverse and forward voltage scans with a scan speed of 1 $V\ s^{-1}$, are shown in Fig. S7.† The average device performance parameters including V_{OC} , J_{SC} , FF, and PCE for over 50 cells are summarized in Table S1.† The histograms of the performance parameters are shown in Fig. 3. It is noted that even with a 40 reaction cycle PEALD SnO_2 ESL (only a few monolayers thickness), the device showed an average V_{OC} higher than 1.0 V. This is ascribed to the complete coverage and the hole-blocking effect of the SnO_2 ESL, as well as the passivation effect of the C_{60} -SAM. As the number of reaction cycles

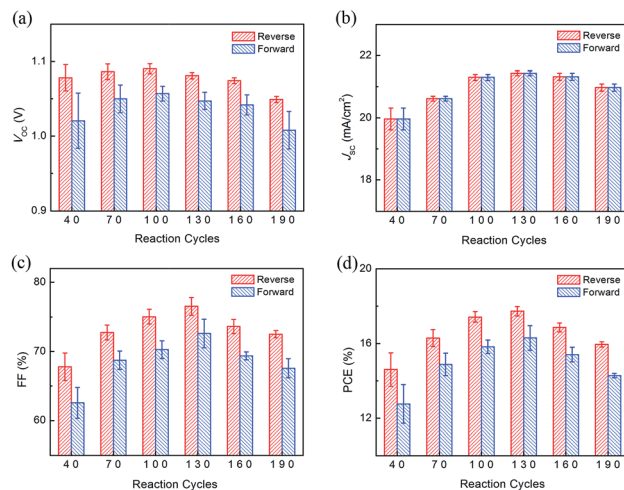


Fig. 3 Histogram of average (a) V_{OC} , (b) J_{SC} , (c) FF, and (d) PCE of PVSCs using the PEALD SnO_2 ESL deposited with various reaction cycles at 100 °C deposition temperature. Error bars represent the standard deviation calculated for 54 devices prepared under the same conditions.

increases, all performance parameters first increase and then decrease. The average PCE reaches the maximum with 130 reaction cycles, which is about 15 nm as determined by spectroscopic ellipsometry. This trend may be understood by the trade-off between the electron transport properties and the hole-blocking ability of SnO_2 ESLs. For increased hole-blocking, thicker SnO_2 ESLs are preferred; however, for improved electron transport, thinner SnO_2 ESLs are required. Consequently, we selected PEALD SnO_2 with 130 reaction cycles (15 nm) to investigate the effect of deposition temperature.

With the number of reaction cycles fixed at 130, we then varied the deposition temperature for PEALD SnO_2 ESLs: 50, 70, 100, 150, and 200 °C. A large number of PVSCs using these SnO_2 ESLs were fabricated. The J - V curves of some representative PVSCs measured under reverse and forward voltage scans are shown in Fig. S8.† The average device performance parameters of over 40 cells are summarized in Table S2.† and their histograms are shown in Fig. 4. It is seen that the average V_{OC} and FF first increase and then decrease as the deposition temperature increases. The J_{SC} appears to increase slightly as the deposition temperature increases, although the change is almost within the order of the statistical variation. The average PCE reaches the maximum value at 100 °C. This is about 20 °C lower than the processing temperature as reported for ozone ALD SnO_2 ESLs.³⁸ It is worth highlighting that even the SnO_2 ESL deposited at 70 °C can produce PVSCs with average efficiency close to 16%. If the processing temperature is further decreased to 50 °C, the device performance decreased dramatically. It is likely that such a low temperature cannot allow the metal precursors to fully react to form high-quality SnO_2 ESLs, even in the presence of plasma-generated reactive species. However, if the processing temperature is too high, the SnO_2 ESLs start to recrystallize, creating pinholes and a rough surface⁴⁰ as shown in Fig. S9,† leading to decreased performance.

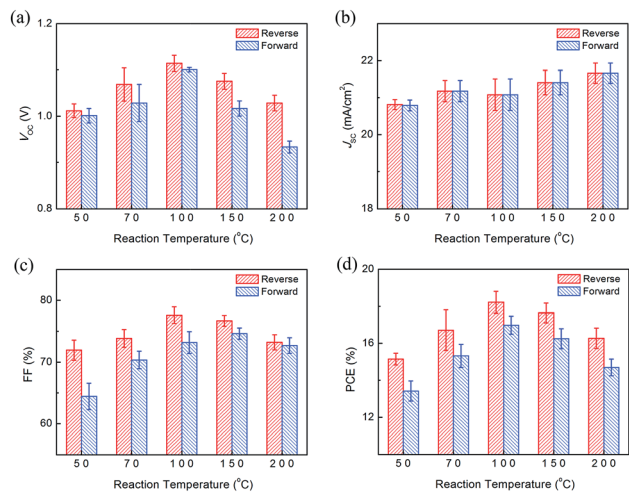


Fig. 4 Histogram of average (a) V_{OC} , (b) J_{SC} , (c) FF, and (d) PCE of PVSCs using the PEALD SnO_2 ESL deposited at various processing temperatures. Error bars represent the standard deviation calculated for 45 devices prepared under the same conditions.

The PVSCs using PEALD SnO_2 ESLs deposited at 100 °C with 130 reaction cycles have achieved an averaged efficiency of $18.21 \pm 0.59\%$, with a J_{SC} of $21.08 \pm 0.42 \text{ mA cm}^{-2}$, a V_{OC} of $1.11 \pm 0.02 \text{ V}$ and a FF of $77.62 \pm 1.34\%$. Our PVSCs exhibited very small J - V hysteretic behaviour. Fig. 5(a) shows J - V curves of a PVSC using a PEALD SnO_2 ESL deposited at 100 °C and with 130 reaction cycles measured under reverse voltage scan with various scan rates. The results indicate that the performance of our devices is relatively independent of the scan rate. The J_{SC} (21.50 mA cm^{-2}) from the J - V curves is very close to the integrated photocurrent (21.20 mA cm^{-2}) from the external quantum efficiency (EQE) as shown in Fig. 5(b). The J - V curves of this PVSC measured under both reverse and forward voltage scan directions are shown in Fig. 5(c), showing almost no hysteresis. The V_{OC} , J_{SC} , FF, and PCE are 1.08 (1.07) V, 21.80 (21.81 mA cm^{-2}), 76.95 (75.48)%, and 18.12 (17.61)%, respectively, when measured under reverse (forward) voltage scan. The corresponding steady-state efficiency is 17.55%, as shown in Fig. 5(d). The current density is 19.12 mA cm^{-2} and the efficiency is 17.55% under a bias of 0.918 V, which is very close to J - V extracted efficiency. It is encouraging that this PVSC also showed good stability when kept under N_2 conditions with relative humidity below 10% and under normal room light. The output power remained unaltered with the storage time, as shown in Fig. 5(e). After being stored for 480 hours, the V_{OC} increased from 1.09 V to 1.11 V, while the FF decreased slightly and the J_{SC} remained unchanged, leading to a negligible change of the PCE. The J - V curves of this PVSC measured under reverse voltage scan after various storage times almost overlapped (Fig. 5(f)). The good stability of PVSCs with the PEALD SnO_2 ESL might be attributable to the negligible catalytic character of SnO_2 and its relative insensitivity to ultraviolet (UV) light (much lower than PVSCs fabricated with TiO_2 (ref. 53 and 54)), which may lead to the negligible degradation of photocurrent observed in our devices.

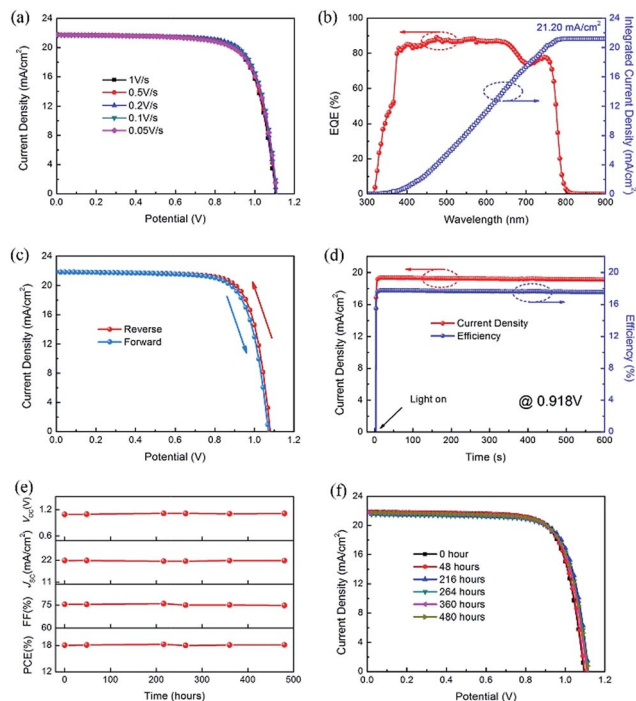


Fig. 5 Hysteresis and stability of a representative PVSC. (a) J - V curves of the perovskite device measured under reverse voltage scan and with different scan speeds. (b) EQE spectrum and the integrated J_{SC} plot. (c) J - V curves measured under reverse and forward voltage scans with a sweep speed of 1 V s^{-1} . (d) Steady-state J_{SC} and PCE of the device with a PEALD SnO_2 ESL at a constant bias of 0.918 V under 100 mW cm^{-2} illumination. (e) Dependence of photovoltaic parameters on the time, and (f) J - V curves measured under reverse voltage scan with time under low humidity conditions.

The low-temperature deposition of efficient SnO_2 ESLs enabled by PEALD is particularly beneficial for fabricating flexible PVSCs. We have fabricated flexible PVSCs on indium-doped SnO_2 (ITO)/polyethylene terephthalate (PET) substrates. The PEALD SnO_2 ESLs were deposited at 100 °C with 130 reaction cycles. Over 30 flexible PVSCs were fabricated, and their average V_{OC} , J_{SC} , FF, and PCE are 1.07 ± 0.04 (1.03 ± 0.05) V, 20.68 ± 0.22 (20.74 ± 0.28) mA cm^{-2} , 70.33 ± 3.18 (61.70 ± 3.42)%, and 15.57 ± 1.14 (13.18 ± 1.00)%, respectively, when measured under reverse (forward) voltage scan. The J - V curves measured under both reverse and forward voltage scans and the EQE spectra of the best-performing PVSC on FTO/glass and ITO/PET substrates are shown in Fig. 5(a) and (b), respectively. The best-performing PVSC fabricated on FTO/glass showed a PCE of 19.03 (18.24)% with a V_{OC} of 1.13 (1.10) V, a J_{SC} of 21.56 (21.55 mA cm^{-2}), and a FF of 78.11 (76.93)% under reverse (forward) scan. Meanwhile, the best-performing flexible PVSC showed a PCE of 16.80 (15.48)% with a V_{OC} of 1.11 (1.09) V, a J_{SC} of 20.50 (20.50 mA cm^{-2}), and a FF of 73.82 (69.28)% under reverse (forward) voltage scan. J - V curves of one flexible PVSC measured under reverse and forward voltage scans with various scan rates are shown in Fig. S10.† Current densities integrated from the EQE spectra are shown in Fig. 6(b), which are 21.14 and 19.61 mA cm^{-2} for the best cells fabricated on FTO/glass and flexible

ITO/PET substrates, respectively. They are in good agreement with those from the J - V curves. It is noteworthy to point out that the V_{OC} of the best flexible PVSC is 1.11 V, only 20 mV lower than that of the best PVSC on the FTO substrate, implying that a pinhole-free and compact SnO_2 ESL also forms on the ITO/PET surface, leading to effective hole-blocking and minimized charge recombination. The absorbance spectra of MAPbI_3 deposited on two substrates, shown in Fig. 6(c), reveal the identical onsets at about 778 nm, indicating similar absorption characteristics irrespective of the substrates (XRD and SEM information of perovskite films deposited on the ITO/PET substrates is provided in Fig. S11†). The lower FF of the flexible device is likely attributable to the relatively higher sheet resistance of the ITO on flexible PET ($\sim 45 \Omega \square^{-1}$), compared with the high-temperature processed FTO electrode on glass ($\sim 15 \Omega \square^{-1}$). The tapping-mode atomic-force microscopy (AFM) images of FTO and ITO shown in Fig. S12† reveal that the FTO also has much larger grain sizes than the ITO. We have also measured the effect of bending fatigue cycles on the device performance as shown in Fig. 6(d). After 200 times of bending with a minimum radius of curvature of 5 mm, the PCE is still 14.00%, approximately 85% of its initial PCE of 16.50%, indicating good flexibility endurance of our PVSCs with the low-temperature PEALD SnO_2 ESL. The significant change of the flexible device performance upon multiple bending originates from the decreased FF, from its initial 71.35 to 61.65% after 200 times of bending. As shown in Fig. 6(d), the FF decreased dramatically with bending cycles, which can also be observed in the J - V curves in Fig. S13(b).† This change is likely ascribable to the increase in the sheet resistance of the ITO/PET flexible substrate, and thus the series resistance of the PVSC, as shown in Fig. S13(a) and (c),† respectively. The increase in the sheet resistance of the ITO/PET substrate with bending time is one of the main causes for the decreased FF. The inset of Fig. 6(d)

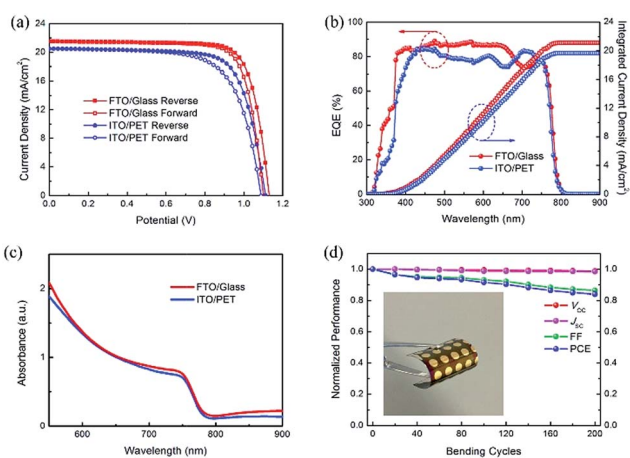


Fig. 6 The best-performing devices based on PEALD SnO_2 coated FTO/glass and ITO/PET substrates: (a) J - V curves under reverse and forward voltage scans. (b) EQE spectra and their corresponding integrated photocurrents. (c) Absorption spectra of perovskite films. (d) Normalized performance parameters of a flexible PVSC versus bending cycles. Photograph of a flexible device after the bending test (inset).

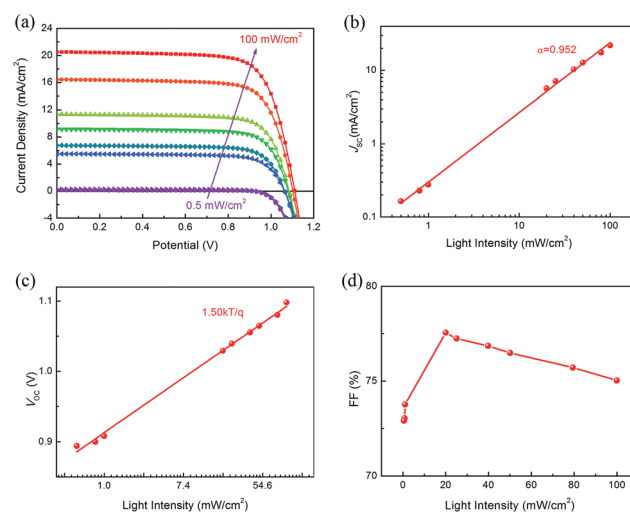


Fig. 7 Light intensity dependence of flexible devices under different illumination.

shows a photograph of our flexible device after the bending test, which still has a shiny and smooth surface without any observable damage.

To further understand the charge recombination mechanism in the flexible devices, light intensity dependence measurements were carried out under different light intensities ranging from 0.5 to 100 mW cm^{-2} as shown in Fig. 7. Fig. 7(a) shows the corresponding J - V curves under the different illumination intensities. The power law dependence of J_{SC} on light intensity ($J \propto I^\alpha$) is shown in Fig. 7(b). A solar device with space charge effects will have a factor $\alpha = 0.75$ while if α is close to 1, there is no space charge.⁵⁵ This flexible device shows a value of $\alpha = 0.952$, indicating a negligible space charge effect. The V_{OC} has a linear relationship with logarithmic light intensity as shown in Fig. 7(c), indicating the presence of Shockley-Read-Hall recombination in the flexible device. Fig. 7(d) displays the dependence of FF on light intensity. Our device configuration on a flexible substrate produces a marginal FF dependence on light intensity, with a maximum FF of 77.50% obtained under 20 mW cm^{-2} illumination, indicating minimized charge recombination at relatively lower light intensity. These results suggest that our flexible device has a low charge recombination rate with no obvious interfacial energy barrier.

Conclusions

We have demonstrated that the PEALD technique could reduce the effective deposition temperature of SnO_2 ESLs to less than 100°C without compromising the PVSC performance. After passivating the surface of SnO_2 ESLs with a C_{60} -SAM, the best PVSCs fabricated on glass substrates have achieved average PCEs and steady-state efficiencies above 18%. The SnO_2 ESLs deposited by PEALD at 70°C enabled the fabrication of PVSCs with average PCEs higher than 17%. Furthermore, the best flexible PVSCs with PEALD SnO_2 ESLs deposited at 100°C have achieved 16.80% PCE, with an average PCE higher than 15%.

Therefore, our results demonstrate the potential of PEALD for synthesizing high quality SnO₂ ESLs at very low temperature for fabricating highly efficient perovskite solar cells.

Acknowledgements

This work is financially supported by the U.S. Department of Energy (DOE) SunShot Initiative under the Next Generation Photovoltaics 3 program (DE-FOA-0000990), National Science Foundation under contract no. CHE-1230246 and DMR-1534686, and the Ohio Research Scholar Program. The work at the National Renewable Energy Laboratory was supported by the U.S. Department of Energy SunShot Initiative under the Next Generation Photovoltaics 3 program (DE-FOA-0000990) under Contract No. DE-AC36-08-GO28308. This research used the resources of the Ohio Supercomputer Center and the National Energy Research Scientific Computing Center, which is supported by the Office of Science of the U.S. Department of Energy under Contract No. DE-AC02-05CH11231. This work also received financial support from the National Basic Research Program of China (2011CB933300), National Science Fund for Distinguished Young Scholars (50125309), and National Natural Science Foundation of China (Grants 51272184 and 91433203).

Notes and references

- 1 A. Kojima, K. Teshima, Y. Shirai and T. Miyasaka, *J. Am. Chem. Soc.*, 2009, **131**, 6050–6051.
- 2 W. S. Yang, J. H. Noh, N. J. Jeon, Y. C. Kim, S. Ryu, J. Seo and S. I. Seok, *Science*, 2015, **348**, 1234–1237.
- 3 D. Bi, W. Tress, M. I. Dar, P. Gao, J. Luo, C. Renevier, K. Schenk, A. Abate, F. Giordano and J.-P. C. Baena, *Sci. Adv.*, 2016, **2**, e1501170.
- 4 N. J. Jeon, J. H. Noh, W. S. Yang, Y. C. Kim, S. Ryu, J. Seo and S. I. Seok, *Nature*, 2015, **517**, 476–480.
- 5 J.-H. Im, C.-R. Lee, J.-W. Lee, S.-W. Park and N.-G. Park, *Nanoscale*, 2011, **3**, 4088–4093.
- 6 M. M. Lee, J. Teuscher, T. Miyasaka, T. N. Murakami and H. J. Snaith, *Science*, 2012, **338**, 643–647.
- 7 S. D. Stranks, G. E. Eperon, G. Grancini, C. Menelaou, M. J. Alcocer, T. Leijtens, L. M. Herz, A. Petrozza and H. J. Snaith, *Science*, 2013, **342**, 341–344.
- 8 W. J. Yin, H. Chen, T. Shi, S. H. Wei and Y. Yan, *Adv. Electron. Mater.*, 2015, **1**, 1500044.
- 9 W. J. Yin, T. Shi and Y. Yan, *Adv. Mater.*, 2014, **26**, 4653–4658.
- 10 W.-J. Yin, T. Shi and Y. Yan, *Appl. Phys. Lett.*, 2014, **104**, 063903.
- 11 W.-J. Yin, T. Shi and Y. Yan, *J. Phys. Chem. C*, 2015, **119**, 5253–5264.
- 12 M. L. Agiorgousis, Y.-Y. Sun, H. Zeng and S. Zhang, *J. Am. Chem. Soc.*, 2014, **136**, 14570–14575.
- 13 M.-H. Du, *J. Phys. Chem. Lett.*, 2015, **6**, 1461–1466.
- 14 J. Burschka, N. Pellet, S.-J. Moon, R. Humphry-Baker, P. Gao, M. K. Nazeeruddin and M. Grätzel, *Nature*, 2013, **499**, 316–319.
- 15 J.-H. Im, I.-H. Jang, N. Pellet, M. Grätzel and N.-G. Park, *Nat. Nanotechnol.*, 2014, **9**, 927–932.
- 16 A. Mei, X. Li, L. Liu, Z. Ku, T. Liu, Y. Rong, M. Xu, M. Hu, J. Chen and Y. Yang, *Science*, 2014, **345**, 295–298.
- 17 N. Ahn, D.-Y. Son, I.-H. Jang, S. M. Kang, M. Choi and N.-G. Park, *J. Am. Chem. Soc.*, 2015, **137**, 8696–8699.
- 18 D. Zhao, M. Sexton, H. Y. Park, G. Baure, J. C. Nino and F. So, *Adv. Energy Mater.*, 2015, **5**, 1401855.
- 19 N. Cheng, P. Liu, S. Bai, Z. Yu, W. Liu, S.-S. Guo and X.-Z. Zhao, *J. Power Sources*, 2016, **319**, 111–115.
- 20 Z. Yu, F. Qi, P. Liu, S. You, K. K. Kondamareddy, C. Wang, N. Cheng, S. Bai, W. Liu, S. Guo and X.-z. Zhao, *Nanoscale*, 2016, **8**, 5847–5851.
- 21 Z. Yu, B. Chen, P. Liu, C. Wang, C. Bu, N. Cheng, S. Bai, Y. Yan and X. Zhao, *Adv. Funct. Mater.*, 2016, DOI: 10.1002/adfm.201504564.
- 22 G. Xing, N. Mathews, S. Sun, S. S. Lim, Y. M. Lam, M. Grätzel, S. Mhaisalkar and T. C. Sum, *Science*, 2013, **342**, 344–347.
- 23 M. Liu, M. B. Johnston and H. J. Snaith, *Nature*, 2013, **501**, 395–398.
- 24 J. H. Heo, H. J. Han, D. Kim, T. K. Ahn and S. H. Im, *Energy Environ. Sci.*, 2015, **8**, 1602–1608.
- 25 C. Wang, Z. Yu, C. Bu, P. Liu, S. Bai, C. Liu, K. K. Kondamareddy, W. Sun, K. Zhan, K. Zhang, S. Guo and X. Zhao, *J. Power Sources*, 2015, **282**, 596–601.
- 26 L. Zuo, Z. Gu, T. Ye, W. Fu, G. Wu, H. Li and H. Chen, *J. Am. Chem. Soc.*, 2015, **137**, 2674–2679.
- 27 J. You, L. Meng, T.-B. Song, T.-F. Guo, Y. M. Yang, W.-H. Chang, Z. Hong, H. Chen, H. Zhou and Q. Chen, *Nat. Nanotechnol.*, 2016, **11**, 75–81.
- 28 J. Song, E. Zheng, J. Bian, X.-F. Wang, W. Tian, Y. Sanehira and T. Miyasaka, *J. Mater. Chem. A*, 2015, **3**, 10837–10844.
- 29 X. Liu, K. W. Tsai, Z. Zhu, Y. Sun, C. C. Chueh and A. K. Y. Jen, *Adv. Mater. Interfaces*, 2016, DOI: 10.1002/admi.201600122.
- 30 H. S. Rao, B. X. Chen, W. G. Li, Y. F. Xu, H. Y. Chen, D. B. Kuang and C. Y. Su, *Adv. Funct. Mater.*, 2015, **25**, 7200–7207.
- 31 Z. Zhu, Y. Bai, X. Liu, C. C. Chueh, S. Yang and A. K. Y. Jen, *Adv. Mater.*, 2016, DOI: 10.1002/adma.201600619.
- 32 T. P. Chou, Q. Zhang and G. Cao, *J. Phys. Chem. C*, 2007, **111**, 18804–18811.
- 33 W. Ke, G. Fang, Q. Liu, L. Xiong, P. Qin, H. Tao, J. Wang, H. Lei, B. Li and J. Wan, *J. Am. Chem. Soc.*, 2015, **137**, 6730–6733.
- 34 Q. Dong, Y. Shi, K. Wang, Y. Li, S. Wang, H. Zhang, Y. Xing, Y. Du, X. Bai and T. Ma, *J. Phys. Chem. C*, 2015, **119**, 10212–10217.
- 35 S. S. Shin, W. S. Yang, J. H. Noh, J. H. Suk, N. J. Jeon, J. H. Park, J. S. Kim, W. M. Seong and S. I. Seok, *Nat. Commun.*, 2015, **6**, 7140.
- 36 J. Yang, B. D. Siempelkamp, E. Mosconi, F. De Angelis and T. L. Kelly, *Chem. Mater.*, 2015, **27**, 4229–4236.
- 37 Q. Hu, J. Wu, C. Jiang, T. Liu, X. Que, R. Zhu and Q. Gong, *ACS Nano*, 2014, **8**, 10161–10167.
- 38 J. P. C. Baena, L. Steier, W. Tress, M. Saliba, S. Neutzner, T. Matsui, F. Giordano, T. J. Jacobsson, A. R. S. Kandada and S. M. Zakeeruddin, *Energy Environ. Sci.*, 2015, **8**, 2928–2934.

- 39 B. Selin Tosun, R. K. Feist, S. A. Campbell and E. S. Aydil, *J. Vac. Sci. Technol., A*, 2012, **30**, 04D101.
- 40 X. Meng, Y. Zhang, S. Sun, R. Li and X. Sun, *J. Mater. Chem.*, 2011, **21**, 12321–12330.
- 41 D. Yang, R. Yang, J. Zhang, Z. Yang, S. F. Liu and C. Li, *Energy Environ. Sci.*, 2015, **8**, 3208–3214.
- 42 S. S. Shin, W.-S. Yang, E. J. Yeom, S. J. Lee, N. J. Jeon, Y.-C. Joo, J. H. Noh, S. I. Seok and I. J. Park, *J. Phys. Chem. Lett.*, 2016, **7**, 1845–1851.
- 43 D. Yang, R. Yang, X. Ren, X. Zhu, Z. Yang, C. Li and S. Liu, *Adv. Mater.*, 2016, **28**, 5206–5213.
- 44 H. B. Profijt, S. E. Potts, M. C. M. van de Sanden and W. M. M. Kessels, *J. Vac. Sci. Technol., A*, 2011, **29**, 050801.
- 45 S. E. Potts, W. Keuning, E. Langereis, G. Dingemans, M. C. M. van de Sanden and W. M. M. Kessels, *J. Electrochem. Soc.*, 2010, **157**, P66–P74.
- 46 C.-C. Chueh, C.-Z. Li and A. K.-Y. Jen, *Energy Environ. Sci.*, 2015, **8**, 1160–1189.
- 47 K. Wojciechowski, S. D. Stranks, A. Abate, G. Sadoughi, A. Sadhanala, N. Kopidakis, G. Rumbles, C.-Z. Li, R. H. Friend, A. K. Y. Jen and H. J. Snaith, *ACS Nano*, 2014, **8**, 12701–12709.
- 48 W. Ke, C. Xiao, C. Wang, B. Saparov, H.-S. Duan, D. Zhao, Z. Xiao, P. Schulz, S. P. Harvey, W. Liao, W. Meng, Y. Yu, A. J. Cimaroli, C.-S. Jiang, K. Zhu, M. Al-Jassim, G. Fang, D. B. Mitzi and Y. Yan, *Adv. Mater.*, 2016, **28**, 5214–5221.
- 49 Y. Chen, B. Li, W. Huang, D. Gao and Z. Liang, *Chem. Commun.*, 2015, **51**, 11997–11999.
- 50 M. Xiao, F. Huang, W. Huang, Y. Dkhissi, Y. Zhu, J. Etheridge, A. Gray-Weale, U. Bach, Y.-B. Cheng and L. Spiccia, *Angew. Chem.*, 2014, **126**, 10056–10061.
- 51 W. Ke, D. Zhao, C. R. Grice, A. J. Cimaroli, J. Ge, H. Tao, H. Lei, G. Fang and Y. Yan, *J. Mater. Chem. A*, 2015, **3**, 17971–17976.
- 52 D. Zhao, W. Ke, C. R. Grice, A. J. Cimaroli, X. Tan, M. Yang, R. W. Collins, H. Zhang, K. Zhu and Y. Yan, *Nano Energy*, 2016, **19**, 88–97.
- 53 T. Leijtens, G. E. Eperon, S. Pathak, A. Abate, M. M. Lee and H. J. Snaith, *Nat. Commun.*, 2013, **4**, 2885.
- 54 C.-H. Wu, *Chemosphere*, 2004, **57**, 601–608.
- 55 V. Mihailetschi, J. Wildeman and P. Blom, *Phys. Rev. Lett.*, 2005, **94**, 126602.